Truncation of the otoferlin transmembrane domain alters the development of hair cells and reduces membrane docking

Aayushi Manchanda[a,†], Josephine A. Bonventre[b,†], Sean M. Bugel[c], Paroma Chatterjee[a], Robyn Tanguay[c], and Colin P. Johnson[a,b,*]

[a]Molecular and Cellular Biology Program, [b]Department of Biochemistry and Biophysics, and [c]Department of Environmental and Molecular Toxicology, Oregon State University, Corvallis, OR 97333

ABSTRACT **Release of neurotransmitter from sensory hair cells is regulated by otoferlin. Despite the importance of otoferlin in the auditory and vestibular pathways, the functional contributions of the domains of the protein have not been fully characterized. Using a zebrafish model, we investigated a mutant otoferlin with a stop codon at the start of the transmembrane domain. We found that both the phenotype severity and the expression level of mutant otoferlin changed with the age of the zebrafish. At the early developmental time point of 72 h post fertilization, low expression of the otoferlin mutant coincided with synaptic ribbon deficiencies, reduced endocytosis, and abnormal transcription of several hair cell genes. As development proceeded, expression of the mutant otoferlin increased, and both synaptic ribbons and hair cell transcript levels resembled wild type. However, hair cell endocytosis deficits and abnormalities in the expression of GABA receptors persisted even after up-regulation of mutant otoferlin. Analysis of membrane-reconstituted otoferlin measurements suggests a function for the transmembrane domain in liposome docking. We conclude that deletion of the transmembrane domain reduces membrane docking, attenuates endocytosis, and results in developmental delay of the hair cell.**

Monitoring Editor
Dennis Discher
University of Pennsylvania

Received: Oct 26, 2020
Revised: Apr 26, 2021
Accepted: May 5, 2021

This article was published online ahead of print in MBoC in Press (http://www.molbiolcell.org/cgi/doi/10.1091/mbc.E20-10-0657) on May 12, 2021.

†Co–first authors.

Conflict of interest: The authors declare no potential conflict of interest.

Author contributions: C.P.J. designed research; J.A.B., A.M., S.M.B., and P.C. performed research; R.L.T. contributed new reagents/analytic tools; J.A.B., A.M., S.M.B., and P.C. analyzed data; A.M., P.C., J.A.B., and C.P.J. wrote the paper.

*Address correspondence to: Colin P. Johnson (colin.johnson@oregonstate.edu).

Abbreviations used: Atoh1a, atonal homologue-1; GAD, glutamate decarboxylase; GFP, green fluorescent protein; LCR, larval chemomotor response; LPR, larval photomotor response; Myo6b, myosin VIb; PI(4,5)P2, 1,2-dioleoyl-sn-glycero-3-phospho-(1′-myo-inositol-4′,5′-bisphosphate); POPC, 1-palmitoyl-2-oleoyl-glycero-3-phosphocholine; POPS, 1-palmitoyl-2-oleoyl-glycero-3-phosphoserine; pvalb9, parvalbumin 9; rtn4rl2a, reticulon 4 receptor like 2a; rtn4rl2b, reticulon 4 receptor like 2b; S100s, S100 calcium-binding protein S; VAMP2, vesicle-associated membrane protein 2.

INTRODUCTION

Vertebrate sensory hair cells serve as the primary receptor cells for hearing and balance. Deflection of stereocilia at the apical end of the cell generates receptor potentials that open Cav1.3 calcium channels and stimulate neurotransmitter release at the afferent neuron synapse (Safieddine *et al.*, 2012; Fettiplace, 2017). Synaptic ribbons located at the presynapse tether vesicles proximal to the membrane, increasing the fidelity of exocytosis (Moser *et al.*, 2020). Neurotransmitter release is calcium regulated and requires the calcium sensor otoferlin (Yasunaga *et al.*, 1999; Roux *et al.*, 2006). In mice, loss of otoferlin results in profound hearing loss, and in humans, mutations in otoferlin are responsible for DFNB9, which accounts for 2–8% of congenital genetic deafness cases.

Structurally, otoferlin is a large (~230 kDa) tail-anchored protein consisting of multiple C2 domains (C2A–C2F), a FerA domain, and a single-pass transmembrane domain (TMD) at the C-terminus (Lek *et al.*, 2012). Consistent with a role in synaptic vesicle release, loss of otoferlin expression abrogates transmission at the ribbon synapse

(Roux *et al.*, 2006). Results of in vitro reconstituted liposome fusion studies suggest that otoferlin may function as a calcium sensor for exocytosis (Johnson and Chapman, 2010). Support for this proposal stems from evidence that multiple C2 domains bind calcium, lipid membranes, and Cav1.3 (Ramakrishnan *et al.*, 2009; Marty *et al.*, 2013; Abdullah *et al.*, 2014; Hams *et al.*, 2017). Further, mutation of the calcium-binding residues in the third C2 domain of otoferlin (C2C) was found to abrogate calcium-triggered liposome fusion in vitro and shift calcium sensitivity of exocytosis in hair cells (Johnson and Chapman, 2010; Michalski *et al.*, 2017). Other studies have linked otoferlin to synaptic vesicle replenishment and vesicle tethering (Pangršič *et al.*, 2010; Vogl *et al.*, 2015). Through direct association with the endocytotic proteins AP2 and myosin VI, otoferlin has also been proposed to participate in clearing of exocytosed material (Heidrych *et al.*, 2009; Jung *et al.*, 2015).

The calcium-binding activity of the otoferlin C2 domains is consistent with a proposed function in calcium-regulated vesicle trafficking and membrane fusion. However, the large size and multiple domains of the protein have made establishing a mechanism for the protein challenging. The large size has also challenged traditional gene delivery strategies (Cepeda *et al.*, 2018; Akil *et al.*, 2019; Rankovic *et al.*, 2021). Recently several organismal model studies have suggested that the C-terminus of otoferlin is minimally necessary for function (Chatterjee *et al.*, 2015; Tertrais *et al.*, 2019). Using a zebrafish model, expression of a truncated form of otoferlin composed of the C2E, C2F, and TMD was found to be sufficient to restore the hearing deficiencies and balance defects associated with loss of endogenous otoferlin (Chatterjee *et al.*, 2015). Studies using a mouse model similarly concluded that the C-terminus of the protein was necessary for rescuing vesicle exocytosis, correcting deficiencies in synaptic ribbon number, and affecting expression of Cav1.3 isoforms (Tertrais *et al.*, 2019). However, this study also found that hearing in otof –/– mice was not restored through expression of a truncated otoferlin (Tertrais *et al.*, 2019). Studies on the otoferlin homologue dysferlin also support the necessity of the C-terminus for protein function in sarcolemma repair (Lek *et al.*, 2013).

Although both in vivo and in vitro studies have highlighted the necessity of the C2 domains of otoferlin, no examination of the TMD has been conducted. To better understand the effects of the TMD, we investigated a mutant zebrafish line harboring an early stop codon in the predicted TMD of the otoferlin gene *otofB*, which is expressed in lateral line neuromasts (Chatterjee *et al.*, 2015).

In this study we find that mutant lateral line hair cells displayed lower expression of *otofB*, reduced endocytosis, and abnormal synaptic ribbon morphology at 72 h post fertilization (hpf). In addition, expression of several hair cell–specific genes were found to be abnormal at 72 hpf. However, mutant otofB expression was increased substantially by 96 hpf, with both synaptic ribbon deficits and transcriptional abnormalities becoming less pronounced with increasing otofB. Regardless of otofB up-regulation, however, deficits in hair cell endocytosis persisted as the organism developed. In addition, abnormal GABA receptor expression was found in both larvae and adult zebrafish, suggesting that otofB mutant up-regulation did not fully compensate for the mutation. Analysis of otoferlin membrane reconstitution measurements suggests a function for the TMD in promoting docking between liposomes. We conclude by proposing a model where the low expression levels and reduced functional activity of the mutant results in lagging development of the hair cell synapse. Up-regulation of the mutant at later time points partially, but not completely, compensates for the deficits.

RESULTS

The otofB mutation

The zebrafish genome encodes two otoferlin genes (otoferlin a, otofA, and otoferlin b, otofB). Previous in situ hybridization studies have demonstrated that *otofb* was present in the otic vesicle as well as the anterior and posterior lateral line neuromasts, while *otofa* expression appears to be restricted to the otic vesicle (Chatterjee *et al.*, 2015). To test the effects of the TMD on otoferlin activity, we studied an otofB mutant zebrafish line (otofsa16297) carrying a point mutation in the otoferlin b gene (Ensembl Gene ID: ENSDARG00000020581, ZFIN ID: ZDB-GENE-110406-5) at position 50320376 (GRCz11) on chromosome 17. The mutation identified through a Targeting-Induced Local Lesions in Genomes (TILLING), was a nonsense [A > T] point mutation that leads to an early stop codon in the fourth amino acid of the predicted TMD (Figure 1A) (Perry *et al.*, 2005). To verify that the mutation resided at the sequence coding for the TMD, both the wild-type (WT) and mutant coding sequences were translated using ExPASy. The resulting protein sequences were entered into TMHMM to predict the location of the single TMD (Supplemental Figure 1) (Sonnhammer *et al.*, 1998). The WT peptide sequence, 1773 amino acids (aa) in total length, was predicted to have one transmembrane helix incorporating amino acids 1740–1762. In contrast, the otofB mutant sequence was 1743 amino acids in total length, with no predicted transmembrane helices, in agreement with the predicted location of the early stop codon.

Otoferlin morphant zebrafish display balance defects and failure to inflate the swim bladder (Chatterjee *et al.*, 2015). To determine whether similar deficiencies exist in the mutant, we compared WT and otofB mutants for anatomical differences. Observations made following multiple spawning events from random group spawns of male and female otofB mutants identified no overt malformations compared with WT counterparts. Further, comparison of the number of inflated swim bladders between the two genotypes revealed no significant differences at 96 hpf (Supplemental Table 1) (Fisher's exact test = 0.4098, wild-type $N = 183$, mutant $N = 162$).

Differences in the expression of wild-type and mutant otoferlin

Zebrafish neuromasts of the lateral line develop functional hair cells by 72–96 hpf (Kindt and Sheets, 2018). Both *otofa* and *otofb* transcripts are expressed at 48 hpf, with increasing expression reaching a plateau at 96 hpf (Chatterjee *et al.*, 2015). To assess otofB expression in neuromasts, we compared immunolabeled neuromast images from mutant and WT larvae (Figure 1, B–H) at 72, 96, and 120 hpf. Because *otofb* is found in lateral line neuromasts, we focused on hair cell bundles present in the supraorbital, occipital, dorsal, and first posterior lateral line (Chatterjee *et al.*, 2015). Representative images of immunolabeled hair cells from both WT and mutant neuromasts at 72, 96, and 120 hpf exhibited a staining pattern consistent with previous immunofluorescence studies, albeit less intense (Figure 1, C–H) (Chatterjee *et al.*, 2015). We compared anti-otoferlin levels between WT and mutant neuromasts by quantitating the average neuromast fluorescence intensity using the CTIF method (Manchanda *et al.*, 2019). To reduce variability due to natural neuromast size/shape differences, we averaged multiple neuromasts from multiple larvae (neuromast $N = 4$ mutant, 6 WT per larva, $N = 4$–8 for WT and mutant larvae each attempt). Analysis revealed a significantly reduced average intensity for otofB neuromasts compared with WT (Figure 1I). This difference was most pronounced at 72 hpf, where immunofluorescence is barely above background level. OtofB intensities at 96 and 120 hpf were closer but still significantly

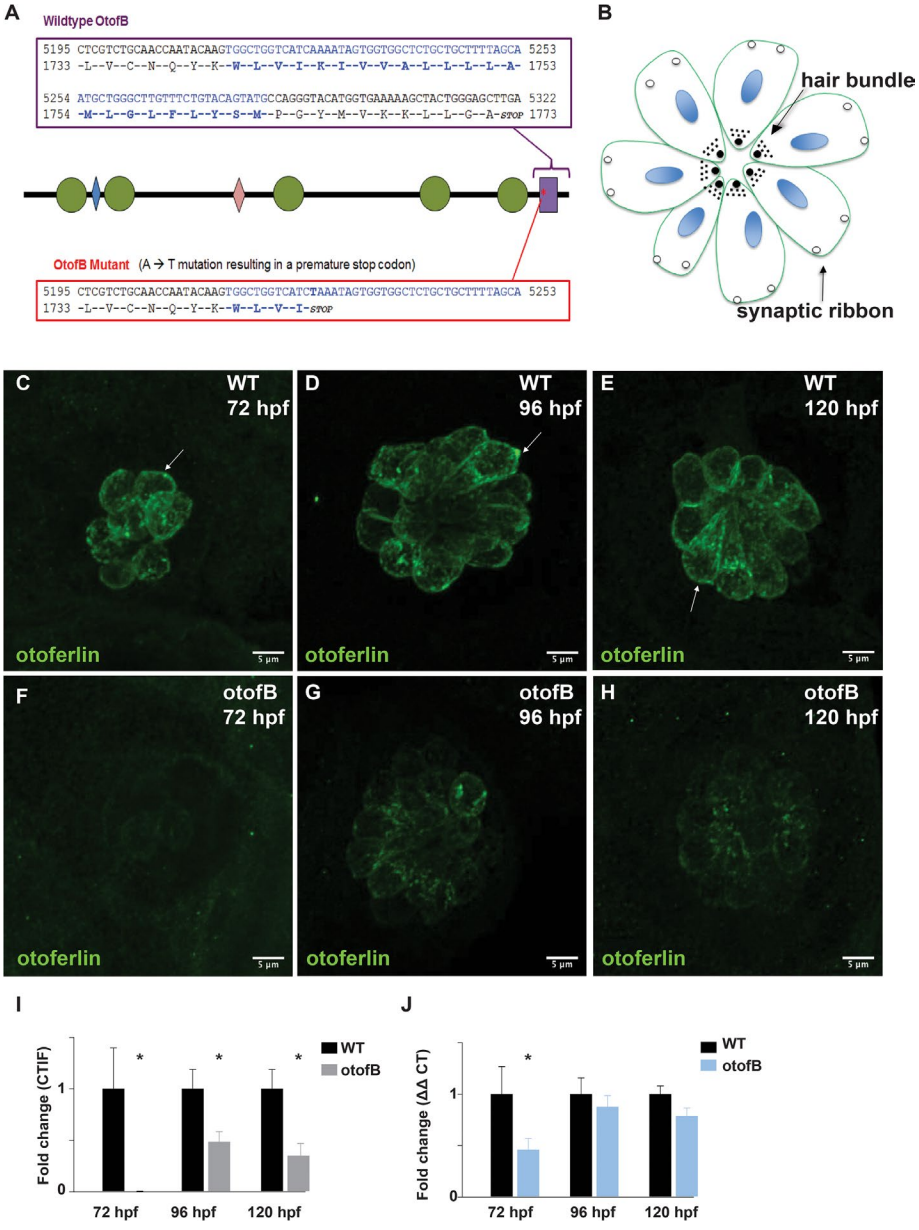

FIGURE 1: The otofb mutation results in reduced otoferlin expression. (A) Schematic of the otofB mutation. Green circles denote C2 domains and blue and pink diamonds denote FerI and FerB domains, respectively. Purple rectangle denotes the TMD. (B) Diagram of a neuromast in the same top-down orientation as the images in panels C–H. (C–E) Representative confocal images of 72 hpf (C), 96 hpf (D), and 120 hpf (E) WT neuromasts stained for otoferlin. Arrows denote the basolateral end of a sensory hair cell. (F–H) Representative confocal images of 72 hpf (F), 96 hpf (G), and 120 hpf (H) mutant neuromasts stained for otoferlin. (I) Quantification of otoferlin in WT and otofB neuromasts (*t* test, $p < 0.001$). $N = 4$ larvae, 4 neuromasts per larvae for both WT and mutant. (J) Quantification of otoferlin mRNA in wild-type and otofb larvae (*t* test, $p < 0.001$). $N = 4$ for both wild type and mutant. Scale bars = 5 µm

lower than with WT. To test whether the decreased otoferlin expression was due to lysosome targeting, we coimmunolabeled with the anti-otoferlin HCS-1 antibody as well as the lysosomal marker LAMP-1. Analysis revealed no difference in colocalization of the markers between WT and mutant, with a Pearson's coefficient for WT = 0.13 ± 0.02, and mutant = 0.15 ± 0.04 ($N = 4$, error bars = SEM) (Supplemental Figure 2).

To determine the mRNA expression level of otofB, we analyzed quantitative PCR (qPCR) results from larvae at 72, 96, and 120 hpf (Figure 1J). At 72 hpf, we found the otofB mutant expression levels were less than 50% that of WT larvae. However, there was no significant difference between mutant and WT at 96 and 120 hpf, which may account for the increased otoferlin immunofluorescence at these time points (Figure 1, I and J). To confirm that otoferlin in the lateral line neuromasts was driven by otofB, and not otofA, in situ hybridization was performed for both transcripts. As previously observed (Chatterjee *et al.*, 2015), otofb, but not otofa, was predominantly expressed in the lateral line neuromasts (Supplemental Figure 3A). In addition, analysis of qPCR results from whole mutant and WT larvae show no up-regulation of otofa expression in mutant larvae, suggesting that otofa is not compensating for loss of otofb in mutants (Supplemental Figure 3).

otofB mutants display reduced endocytosis

Targeted morpholino knockdown of otoferlin results in decreased endocytotic uptake of the fluorescent marker mCLING into neuromasts (Figure 2, A and B) (Manchanda *et al.*, 2019). mCLING is a dye with selective uptake via endocytosis that has been used previously in mouse and zebrafish hair cells (Revelo *et al.*, 2014, Manchanda *et al.*, 2019). To determine the effect of the otofB mutation on endocytosis, we compared WT and mutant zebrafish exposed to mCLING at 72, 96, and 120 hpf (Figure 2, C–F; Supplemental Figure 4). Analysis of the uptake revealed a marked decrease in the amount of mCLING associated with the mutant as compared with developmentally time-matched WT larvae (Figure 2, C–F). At 72 hpf, mutant neuromast mCLING intensity was only 34.9% that of WT (Figure 2G). However, at 96 hpf, mCLING uptake in mutant neuromasts was approximately 72.8% that of WT, and at 120 hpf mutant intensity was only 86% of WT (Figure 2, H and I). No significant differences in intensity between larvae within the WT group or between larvae of the mutant group were observed. We conclude that up-regulation of the otofb mutant at 96 hpf partially restores endocytosis; however, some deficiency persists through 120 hpf.

Decreased Ribeye and Vglut3 expression in otofb mutants

Morpholino-induced knockdown of otoferlin results in fewer synaptic ribbons relative to control (Manchanda *et al.*, 2019). Morphants also form larger anti-Ribeye puncta compared with control, which may represent single, large synaptic ribbons, or tightly spaced clusters of ribbons. To test for the effect of the otofB mutation on the synaptic ribbon, we analyzed images of Ribeye immunolabeled lateral line neuromasts at 72, 96, and 120 hpf (Figure 3, A–F). We found that otofB hair cells displayed a similar number of Ribeye

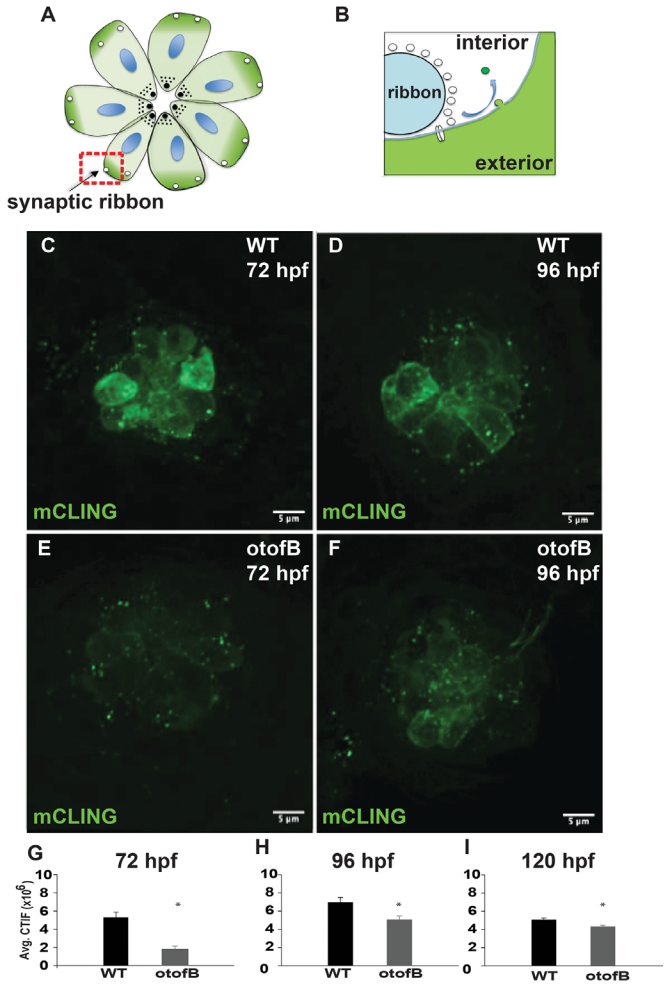

FIGURE 2: The otofB mutation results in reduced mCLING uptake. (A) Diagram of a neuromast in the same top-down orientation as the images in panels C–F. (B) Magnified view of a ribbon synapse highlighted in red in panel A. Endocytosis results in mCLING incorporation from the cell exterior into the vesicle lumen (green). (C, D) Representative confocal images of (C) 72 hpf and (D) 96 hpf mCLING-stained wild-type lateral line neuromasts. (E, F) Representative confocal images of (E) 72 hpf and (F) 96 hpf mCLING-stained mutant lateral line neuromasts. (G) Quantification of average mCLING dye associated with 72 hpf neuromasts of wild-type and otofB zebrafish (*t* test, $p < 0.001$). (H) Quantification of average mCLING dye associated with 96 hpf neuromasts of wild-type and otofB zebrafish (*t* test, $p < 0.001$). $N = 6$ larvae, 4 neuromasts per larvae for both wild type and mutant. Scale bars = 5 µm. (I) Quantification of average mCLING dye associated with 120 hpf neuromasts of wild-type and otofB zebrafish (*t* test, $p < 0.001$). $N = 4$ WT larvae, 3 mutant larvae, 4 neuromasts per larvae. Scale bars = 5 µm.

immunolabeled puncta relative to WT at all time points tested (Figure 3G) (Manchanda *et al.*, 2019). Although puncta number appeared unaffected, otofB neuromasts displayed significantly smaller and dimmer puncta relative to WT at 72 and 96 hpf (Figure 3, H and I). However, at 120 hpf both puncta size and intensity in otofB mutants and WT larvae were not significantly different. We also examined *ribeye b* mRNA transcript levels in mutant and WT larvae and found that although there was no significant difference in *ribeye b* expression at 72 hpf, *ribeye b* transcripts were higher in otofB mutant larvae at 96 and 120 hpf relative to control (Figure 3J).

Expression of the synaptic vesicle protein Vglut3 was also abnormal in otofB mutant larvae (Figure 4, A–F). Quantitation of the average anti-Vglut3 fluorescence intensity revealed less staining in otofB mutant neuromasts relative to WT at all three time points tested (Figure 4G). Comparison of whole larvae mRNA transcript levels between WT and mutant revealed significantly less *vglut3* in mutants at 72 hpf, but no difference at 96 or 120 hpf (Figure 4H). Overall, we conclude that the effects of the otofB mutation on synaptic ribbons and Vglut3 appear most prominent at 72 hpf and less pronounced at later time points when otofB expression levels increase.

otofB mutants display altered expression of hair cell transcripts

Otoferlin morphant larvae exhibit abnormal transcriptional expression of several hair cell–specific genes including myosin VIb (*myo6b*), parvalbumin (*pvalb9*), *s100s*, and the Nogo-related proteins *rtn4rl2a* and *rtn4rl2b* (Manchanda *et al.*, 2019). We therefore sought to compare the expressions of several neuromast hair cell markers between mutant otofB and WT larvae (Figure 5). We found that whole larvae otofB mutant samples exhibited significantly lower levels of *myo6b*, *ret4rl2a*, *ret4rl2b*, and *s100s* at 72 hpf relative to developmentally matched WT, similar to results described for otoferlin morphants. One difference between morphants and the mutant was the expression of *pvalb9*. Where expression of *pvalb9* was reported to be significantly increased in morphants relative to control, we found expression of *pvalb9* in the otofB mutant was significantly lower compared with WT (Figure 5D) (Manchanda *et al.*, 2019). By 120 hpf, there were no significant differences in expression for any of the hair cell–related genes tested between the otofB mutant and WT. No difference in the expression of *atoh1*, a transcription factor involved in development of neuromasts, was found between otofB and WT at any time point tested (Figure 5B).

Truncation of the TMD reduces expression of otoferlin in cell culture

To further probe the effect of truncation of the TMD, we compared HEK cells transfected with mouse WT otoferlin or a mutant otoferlin that mimics the otofb truncation (oto ΔTMD). Fluorescence microscopy revealed that both green fluorescent protein (GFP)-tagged WT and mutant otoferlin colocalized with cells cotransfected with VAMP2, suggesting that both WT and oto ΔTMD trafficked to intracellular membranes (Figure 6A). After verifying expression, we compared the WT and oto ΔTMD immunofluorescence intensities for differences (Figure 6, B and C). Quantitation of the otoferlin intensity revealed significantly lower levels of oto ΔTMD relative to the WT (Figure 6C). We also probed for WT and oto ΔTMD after fractionation of lysate into membrane and cytosolic fractions. Higher levels of WT protein and a larger fraction of WT protein in the membrane fraction was observed relative to oto ΔTMD (Supplemental Figure 5).

The TMD enhances membrane docking in an in vitro liposome assay

The C2F domain of otoferlin resides adjacent to the TMD and binds preferentially to PI(4,5)P2 lipids (Padmanarayana *et al.*, 2014). We therefore tested whether a TMD-anchored C2F domain could bridge membranes using a liposome docking assay (Figure 7A). For comparison, we also tested a soluble C2F domain lacking a TMD. In this assay, streptavidin beads conjugated to liposomes with 5% PIP2 (5:25:60:5:5 PIP2, POPS, POPC, rhodamine-PE, biotin-PE) are targeted by either C2F-proteoliposomes (25:60:10:5 POPS, POPC, POPE, NBD-PE) labeled with NBD-PE or a soluble C2F mixed with NBD-PE–labeled liposomes (Figure 7A). After exposure for 1 h,

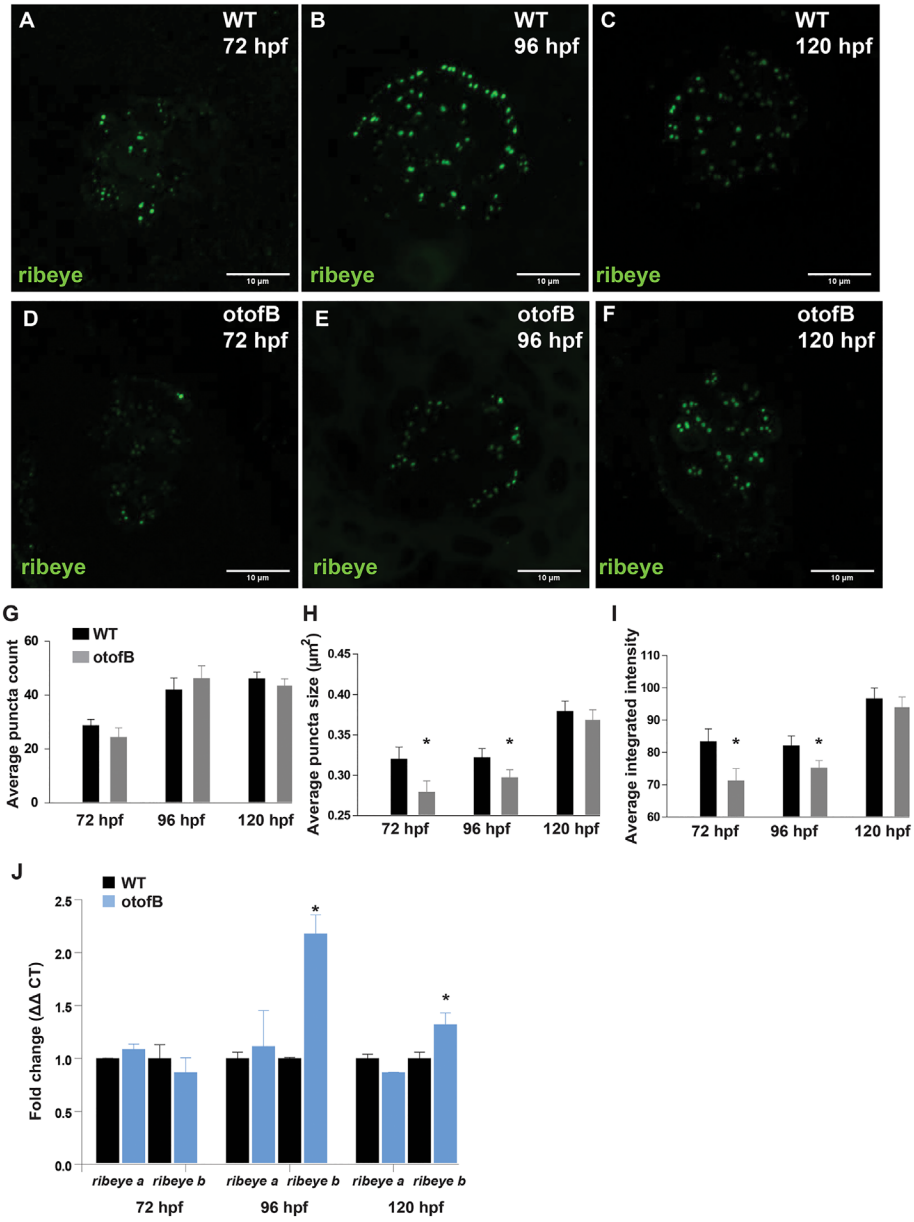

FIGURE 3: The otofB mutation results in reduced expression of Ribeye in neuromasts. (A–C) Representative confocal images of 72 hpf (A), 96 hpf (B), and 120 hpf (C) wild-type neuromasts stained for Ribeye. (D–F) Representative confocal images of 72 hpf (D), hpf 96 (E), and 120 hpf (F) mutant neuromasts stained for Ribeye. (G) Average puncta count in Ribeye-stained wild-type and otofB neuromasts (*t* test, $p < 0.001$). $N = 4$ WT and 6 mutant larvae, 4 neuromasts per larvae for both WT and mutant. (H) Average Ribeye puncta sizes in μm² for wild-type and otofB mutant neuromasts. (I) Average integrated intensity of Ribeye puncta for wild-type and otofB mutant neuromasts. (J) Quantification of Ribeye a and Ribeye b mRNA transcript expression at 72, 96, and 120 hpf in WT and otofB mutant larvae (*t* test, $p < 0.001$). $N = 4$ for both wild type and mutant. Scale bars = 5 μm.

the ratios of NBD signal between the pelleted sample and supernatant sample were compared (Figure 7B). We found a significant increase in the NBD fraction in the pellet for samples with the tethered C2F-TMD relative to no-protein controls. Notably the fraction of NBD in pellet samples with soluble C2F was significantly lower compared with the membrane-tethered sample (Figure 7B). This suggests that the TMD significantly enhances *trans* membrane docking between the proteoliposome and the PI(,5)P2-liposome. SDS–PAGE analysis verified that the C2F and C2F-TMD proteins in the docking assay bound the PI(4,5)P2 liposomes (Supplemental Figure 6). To test whether the observed interaction was sensitive to negatively charged lipids like PI(4,5)P2, we repeated the experiment with streptavidin beads conjugated to liposomes lacking PI(4,5)P2 (90:5:5 POPC, rhodamine-PE, biotin-PE). We found that the NBD fractions in the pellet for both protein samples were not significantly different from the no-protein control (Figure 7C). This is consistent with the reported PI(,5)P2 lipid-binding selectivity of the C2F domain (Padmanarayana *et al.*, 2014).

otofB mutants display abnormal transcript levels of GABAR subunits and GAD

A recent study concluded that otoferlin both directly interacts with glutamate decarboxylase (GAD) and affected GAD transcript levels (Sarro *et al.*, 2008; Noh *et al.*, 2010; Wu *et al.*, 2015). We therefore measured GAD and GABA receptor subunit expression levels in WT and mutant larvae (Figure 8). We found that otofB mutants exhibited significantly lower levels of GABA receptor transcripts at 72, 96, and 120 hpf relative to developmentally matched WT (Figure 8, A–C). Differences in GABA receptor subunit transcripts between mutant and WT persisted through adulthood, with 18-mo-old zebrafish displaying abnormal levels of *gabra1*, *gabbr1a*, *gabbr1b*, *gabra6a* compared with age-matched WT samples (Figure 8D). GAD levels were also abnormal in otofB mutants, with significantly reduced expression of *gad2* compared with WT at both 72 hpf and 18 mo (Figure 8, A and D). We conclude that abnormalities in GABA receptor expression are not corrected by the observed up-regulation of the otofB gene and that this abnormality continues through adulthood.

Altered behavior and hyperactive responses in otofB mutants

Two larval locomotor-based behavioral assays were used to determine whether otofB mutants exhibit altered behaviors related to the aberrant GABAR and GAD expression. The larval photomotor response (LPR) assay was used to determine general behavioral activity in WT and otofB mutants. For this assay, locomotor activity was evaluated in 4 d post fertilization (dpf) larvae following phototransitions from light to dark. Typical hyperactive responses are observed in the dark period, whereas low levels of resting activity are normally observed in the light phase. Overall, typical LPR responses were observed in both WT and otofB genotypes, characterized by hyperactive responses in the dark phase and low levels of activity in the light phase (Figure 9, A and B). Statistical differences were found between genotypes when analyzing the data within each specific

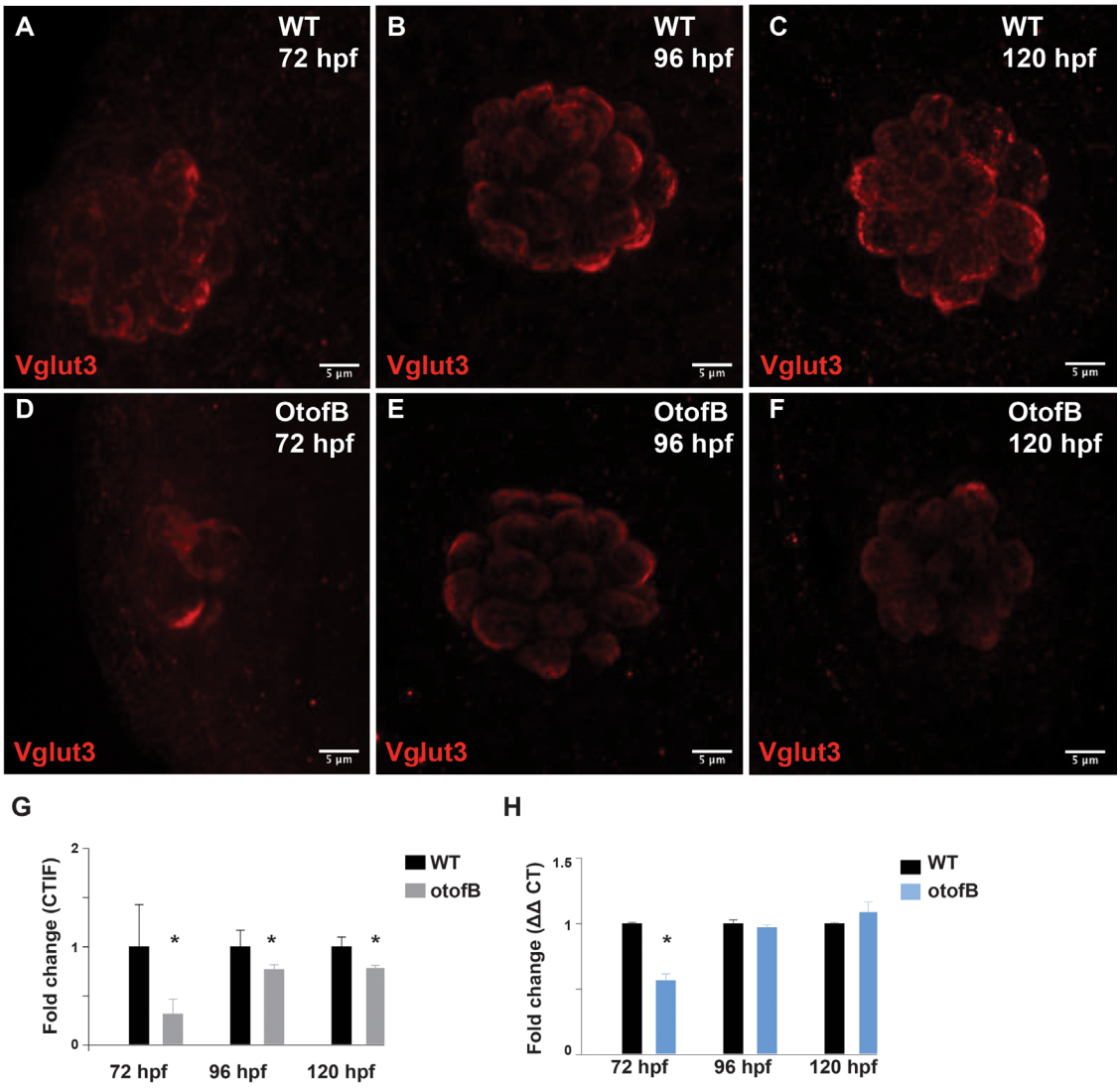

FIGURE 4: The otofB mutation results in reduced Vglut3 in neuromasts. (A–C) Representative confocal images of 72 hpf (A), 96 hpf (B), and 120 hpf (C) WT neuromasts stained for Vglut3. (D–F) Representative confocal images of 72 hpf (D), 96 hpf (E), and 120 hpf (F) mutant neuromasts stained for Vglut3. (G) Quantification of Vglut3 in WT and OtofB neuromasts (*t* test, $p < 0.001$). $N = 4$ larvae, four neuromasts per larvae for both WT and mutant. (H) Quantification of Vglut3 mRNA transcripts in WT and OtofB larvae (*t* test, $p < 0.001$). $N = 4$ for both WT and mutant. Scale bars = 5 µm.

minute throughout the time course (Figure 9A). When analyzing the average activity data within each photoperiod, statistical differences were found in the light phases of trials 4 and 5 (Figure 9B). This indicates that otofB mutants have an abnormal rest phase following a stimulus and suggests a modest overall hyperactive phenotype.

Following the LPR study, the more specific larval chemomotor response (LCR) assay was used to determine whether genotypes differed in locomotor responses to a $GABA_A$ receptor–specific antagonist in 4 d postfertilization larvae (Figure 9, C and D). Picrotoxin (PTX) was used to induce robust changes in locomotor activity through $GABA_A$ receptor inhibition. Differences between WT and mutant responses to PTX were found in the time bins starting at $t =$ 21–30 min after application of PTX (Figure 9D). The control groups did not differ between genotypes in any time bin in the LCR. The significant differences between the treated genotypes indicated a more robust hyperactive response to PTX in otofB mutants relative to WT controls treated with PTX. This hyperactive phenotype is consistent with the abnormal GAD and GABA receptor subunit expression levels detected by qPCR. Overall, we conclude that there are functional $GABA_A$ receptor–specific differences in behavior for the otofB mutant relative to WT.

DISCUSSION

The C2 domains of otoferlin have been the focus of several studies. In this report we characterized the role of the TMD of otoferlin using in vitro and in vivo systems. We found that the TMD plays an important role for proper expression of the protein. Specifically, truncation of the TMD reduced expression in both mutant zebrafish and mammalian cell culture. The low expression levels of otofB appear to result in a developmental delay for the neuromasts, similar to delays linked to other gene mutants (Zallocchi *et al.*, 2012). Using a zebrafish model we found that mutant otoferlin expression was less than WT at 72 hpf, and deficits in endocytosis, mistrafficking of Vglut3, and smaller and less intense Ribeye puncta were observed. In addition, whole 72 hpf mutant larvae displayed lower expression levels of several neuromast genes. In agreement with the conclusion

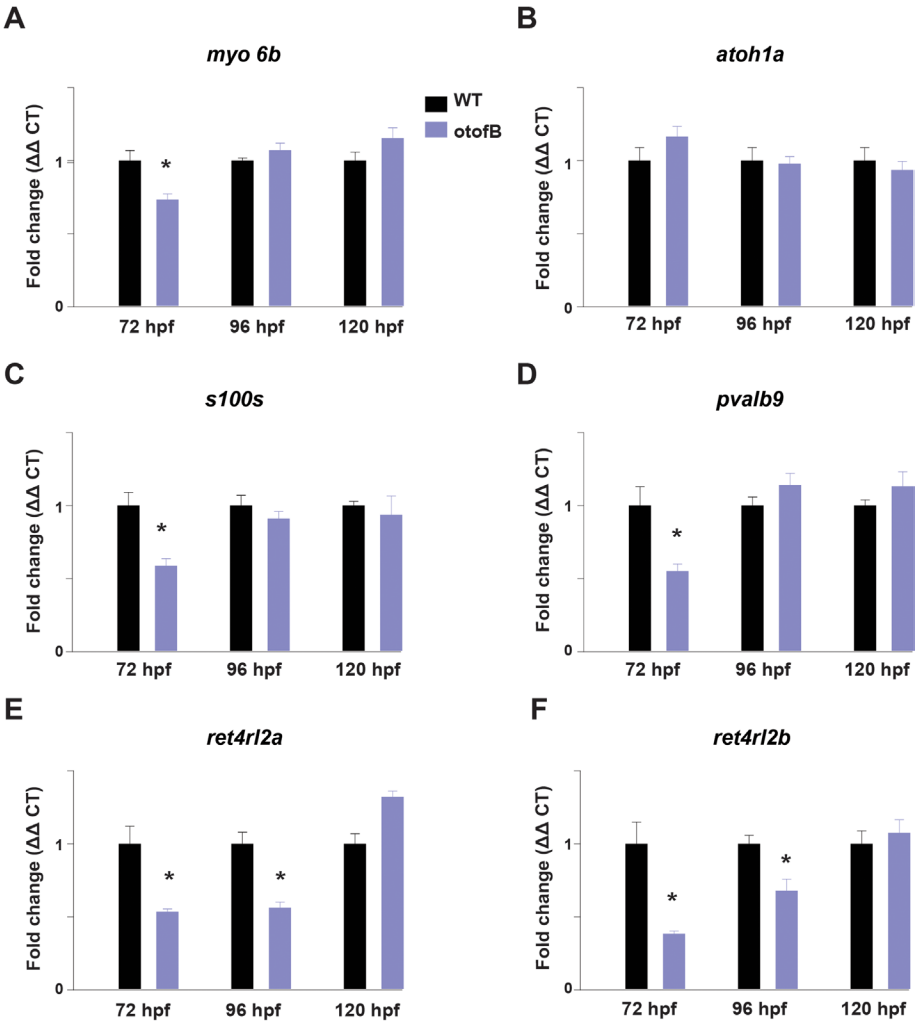

FIGURE 5: The otofB mutation results in altered expression of hair cell–related transcripts. (A–F) Quantification of mRNA by qRT-PCR for myo6b, atoh1a, s100s, pvalb9, ret4rl2a, ret4rl2b in wild-type and otofB larvae at 72, 96, and 120 hpf. (A) Quantification of myo6b mRNA, (B) quantification of Atoh1a mRNA, (C) quantification of s100s mRNA, (D) quantification of pvalb9 mRNA, (E) quantification of rtn4rl2a mRNA, (F) quantification of rtn4rl2b mRNA in wild-type and otofB larvae at 72, 96, and 120 hpf (*t* test, $p < 0.001$). $N = 4$ for both WT and mutant, with each N as a composite of 20–30 larvae. The data presented are representative of three experimental replicates for each time point. Error bars are SEM.

complexes despite the loss of membrane anchoring.

Using an in in vitro assay, we found that removal of the TMD severely reduced otoferlin-mediated docking between liposomes. Without membrane anchoring by the TMD, the soluble C2F domain could not bridge the two sets of liposomes as effectively as the tethered protein. We speculate that the loss of docking we observed in our in vitro assay could contribute to the observed mCLING loading deficits observed in mutant hair cells. TMD anchoring plays a critical role for other synaptic proteins, including the neuronal calcium sensor synaptotagmin (Lee and Littleton, 2015). For example, in synaptotagmin knockout cells, expression of exogenous synaptotagmin lacking a TMD in a null background did not restore synchronous release (Lee and Littleton, 2015). In our assay, the liposome docking activity of C2F-TMD required the presence of PI(4,5)P2, in agreement with a role for this lipid in directing otoferlin to the cell membrane. A similar role has been proposed for PI(4,5)P2 in directing synaptotagmin-mediated docking of synaptic vesicles in hippocampal neurons (Chen *et al.*, 2021).

Finally, WT and mutant expressed different levels of GAD and several GABA receptors, and this difference in expression was observed in both larvae and adult stages. Long-term changes in GABA receptor and GAD expression in response to hearing loss were previously reported in mouse models (Kotak *et al.*, 2008; Sarro *et al.*, 2008). Otoferlin has also been reported to directly interact with the membrane-associated isoform of GAD, and otoferlin expression levels have been reported to correlate with GAD expression in mammalian cells (Wu *et al.*, 2015). We found abnormal expression of gad2 and several GABA receptor subunit isoforms in whole larvae at early developmental time points (72, 96, 120 hpf), as well as in adult zebrafish brains, suggesting that the mutation has long-term effects and that the observed up-regulation of the otofB mutant gene between 72 and 96 hpf does not fully correct the phenotype. Further, the otofB mutant larvae exhibited increased GABA antagonist sensitivity in two behavioral assays, suggesting a GABAnergic deficiency. Further studies may be warranted to explore the potential for abnormal adult behavior from aberrant GABA signaling owing to the loss of the C-terminus TMD of otoferlin.

In summary, we conclude that the presence of the TMD influences otoferlin expression levels within the hair cell. These conclusions are based on findings that loss of the TMD results in lower otoferlin expression levels and developmental delay of zebrafish neuromasts. In vitro measurements indicate that tethering of otoferlin to liposomes by the TMD increased the liposome docking activity of otoferlin. A reduction in protein tethering and membrane docking could contribute to the observed deficiencies in endocytosis.

that truncation of the TMD lowers expression; we also found that this truncation resulted in lower levels of otoferlin in transfected mammalian cells.

In 96 hpf larvae, up-regulation of mutant otoferlin correlated with the restoration of synaptic ribbon characteristics and more WT-like gene transcription. In addition, endocytosis increased at 96 hpf, although some endocytotic deficiency persisted. These observations suggest that compensatory up-regulation of mutant otoferlin may be responsible for the observed change in phenotype. By contrast, a previous study on morpholino knockdown zebrafish found that the continuous suppression of otoferlin expression results in a phenotype similar to that of our mutant at 72 hpf, which was invariant over the span of their study (Manchanda *et al.*, 2019). Otoferlin has been proposed to act as a multivalent binding protein, interacting with both exocytotic and endocytotic proteins (Hams *et al.*, 2017). It is plausible that the increase in otofB copy number may aid in the assembly of protein

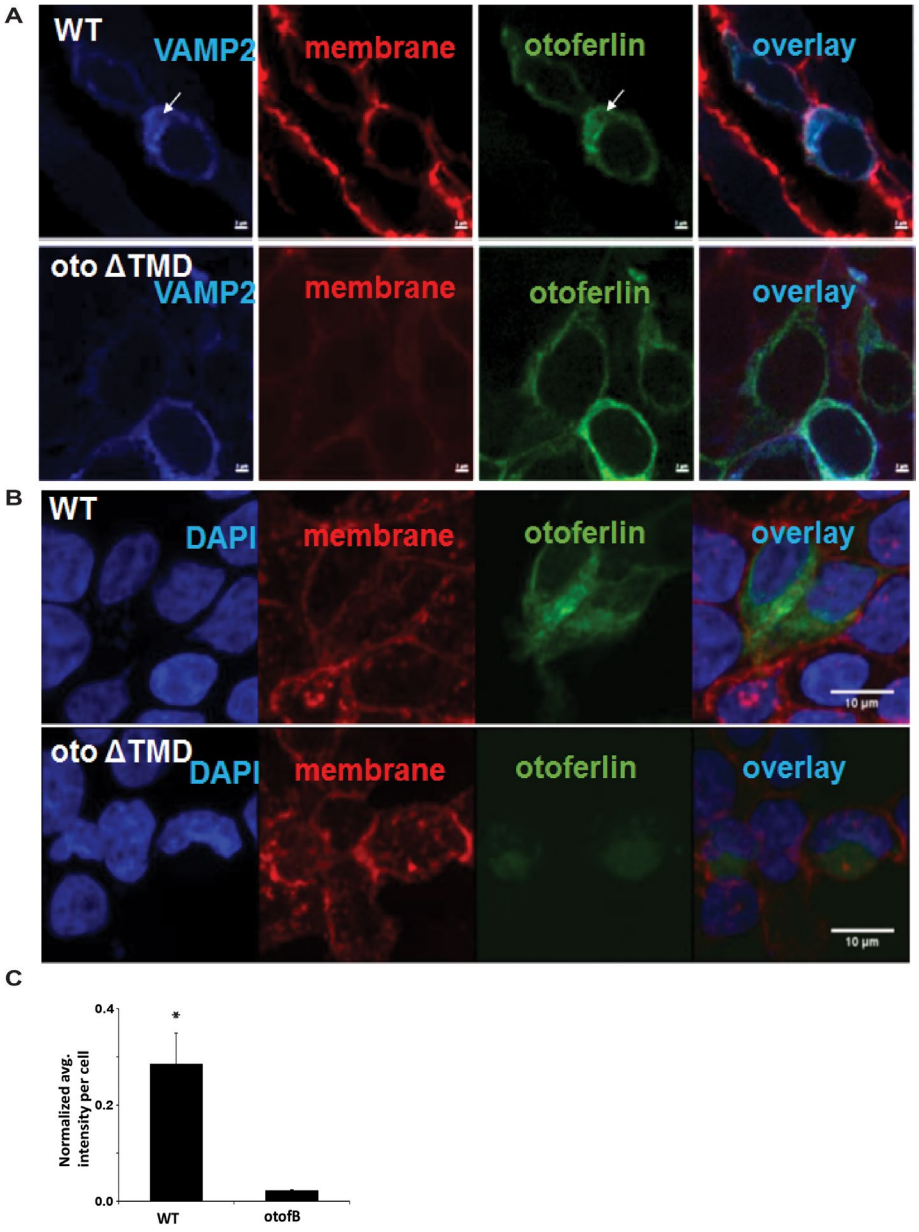

FIGURE 6: Loss of the TMD reduces expression of otoferlin in cell culture. (A) Representative images of cells transfected with CFP-VAMP and either WT mouse otoferlin or ΔTMD, a mouse otoferlin with a mutation matching the otofB mutation. (B) Representative images of cells labeled with 4′,6-diamidino-2-phenylindole (blue), wheat germ agglutinin for the cell membrane (red), and otoferlin (green). (C) Quantitation of the intensity of otoferlin from transfected HEK cells (*t* test, $p < 0.001$). Scale bar for A and B = 2 μm, and 10 μm for C and D.

MATERIALS AND METHODS

Request a protocol through *Bio-protocol*.

Zebrafish husbandry and embryo handling

Adult zebrafish (*Danio rerio*) were housed at the Sinnhuber Aquatic Research Laboratory (SARL) at Oregon State University (Corvallis, OR) and maintained on a recirculating system with water temperature of 28 ± 1°C on a 14:10 light/dark cycle. All experiments were conducted in adherence with the Guide for the Care and Use of Laboratory Animals of the National Institutes of Health using protocols approved by the Oregon State University Institutional Animal Care and Use Committee (IACUC). Standard husbandry procedures were used for all embryos (Westerfield, 2007).

otofsa16297 mutant line

otofb mutant zebrafish (otofsa16297) carry a point mutation in otoferlin b (Ensemble Gene ID: ENSDARG00000020581, ZFIN ID: ZDB-GENE-110406-5) at position 50320376 (GRCz11) on chromosome 17. The mutation was originally identified through a TILLING project. For generating mutants, *N*-ethyl-*N*-nitrosourea (ENU)-mutagenized zebrafish are screened and mutants identified (Wienholds *et al.*, 2003; Kurowska *et al.*, 2011). A nonsense [A > T] point mutation leads to an early stop codon in the fourth amino acid of the predicted TMD. Heterozygous otofsa16297, produced via in vitro fertilization of wild-type AB eggs with otofsa16297 cryopreserved sperm, were purchased from the Zebrafish International Resource Centre (Eugene, OR) and raised to adulthood at SARL on a flow-through system with water temperature of 28 ± 1°C on a 14:10 light/dark cycle. Offspring of heterozygous carriers were genotyped for the otofsa16297 point mutation with genomic DNA isolated from caudal fin clips as previously described (Bonventre *et al.*, 2019; Manchanda *et al.*, 2019). PCR products were sent for sequencing to confirm the genotype of otofB+/+ and otofsa16297, hereafter wild type (WT) and mutant, respectively. The mutant and WT lines were maintained through subsequent group spawns of random male and females.

Computational analysis of WT and mutant sequences

Web-based programs were used to determine the impact of [A > T] point mutation on translation. ExPASy (https://web.expasy.org/translate/) was used to computationally verify the resulting translated sequence in the otofB mutant. The resulting mutant sequence, as well as the WT sequence, were entered into the transmembrane helix domain predictor software TMHMM.

RNA isolation and qPCR analysis

Total RNA was isolated from whole larvae at 72 (day 3), 96 (day 4), and 120 (day 5) hpf using RNAzol RT (Molecular Research Centre, Cincinnati, OH). Each RNA sample was a composite of approximately 20–30 larvae. RNA was converted to cDNA using the Applied Biosystems High-Capacity cDNA Reverse Transcription kit (Life Technologies, Carlsbad, CA), and qPCR for target genes was performed using Power SYBR Green PCR Master Mix with a 7500 Fast Real-Time (Applied Biosystems, Foster City, CA). Primers were purchased from Integrated DNA Technologies (Coralville, IA) as described previously (Cocco *et al.*, 2017; Manchanda *et al.*, 2019). Relative gene expression was quantified using the ΔΔCt method using β-actin as a housekeeping gene for normalization (Pfaffl, 2001).

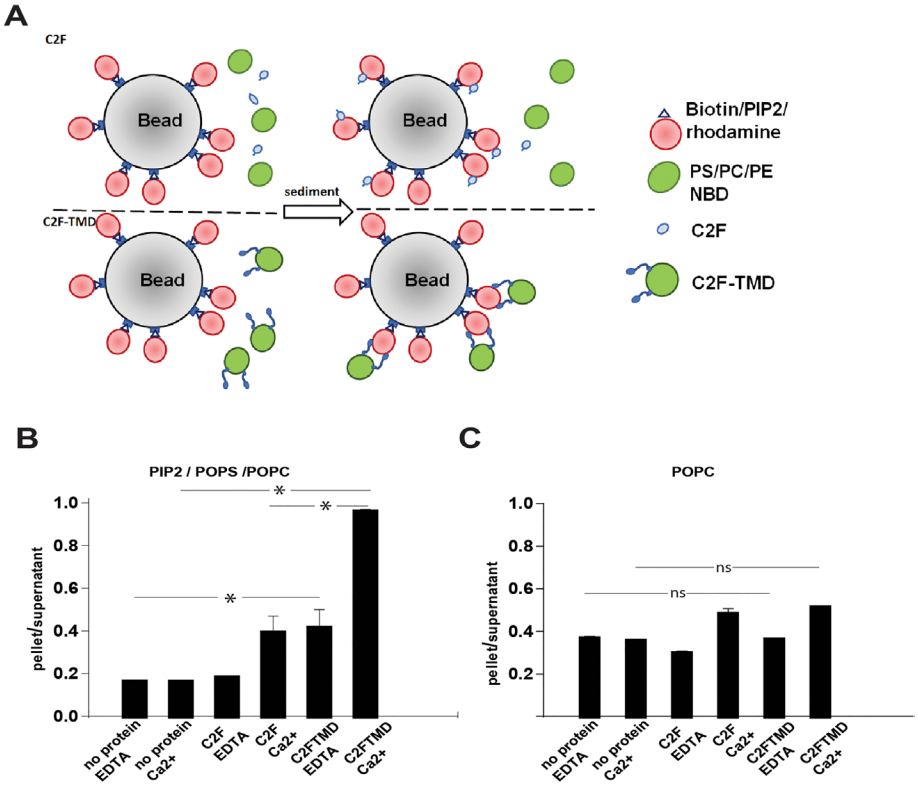

FIGURE 7: Reconstituted otoferlin docks adjacent liposomes. (A) Diagram of the pull-down system. Rhodamine-labeled liposomes are conjugated to streptavidin beads and mixed with either NBD liposomes and soluble C2F (top) or C2F-TMD proteoliposomes labeled with NBD (bottom). (B) Quantitation of liposome sedimentation assay with bead-conjugated liposomes with PI(4,5)P2 (5:25:60:5:5 PIP2, POPS, POPC, rhodamine-PE, biotin-PE) (*t*-test, $p < 0.001$). (C) Quantitation of liposome sedimentation assay with bead-conjugated liposomes without negatively charged lipids (90:5:5 POPC, rhodamine-PE, biotin-PE) (*t*-test, $p < 0.001$). $N = 4$.

Whole-mount in situ hybridization

In situ hybridization was performed on WT and mutant embryos using digoxigenin (DIG)-labeled antisense RNA probes designed to hybridize to a unique regions of the otofB and otofA zebrafish mRNA as previously described (Chatterjee *et al.*, 2015). The design and detection of the probe with anti-DIG alkaline phosphatase–conjugated antibody were performed as previously described (Chatterjee *et al.*, 2015). Stained embryos were imaged on a Keyence BZ-X fluorescence microscope.

Whole-mount immunohistochemistry

WT and mutant zebrafish larvae were collected at stage-specific time points and fixed in 4% paraformaldehyde overnight at 4°C. Fixed larvae were washed with phosphate-buffered saline (PBS) + 0.1% Tris (PBST) 4 × 5 min and then permeabilized on ice with 0.005% trypsin in PBS for 6 min followed by 3 × 5 min PBST washes and a 10 min postfix with 4% paraformaldehyde. After 3 × 5 min PBST washes, samples were blocked with 6% normal goat serum and 1% bovine serum albumin in PBST for 2–4 h at room temperature (RT). Samples were then incubated with primary antibodies diluted in PBS buffer overnight at 4°C. Samples were washed 3 × 5 min with PBST followed by incubation with secondary antibodies (1:1000) coupled to Alexa Fluor 488 (anti-mouse) or Alexa Fluor 594 (anti-rabbit) (Invitrogen), washed 3 × 5 min with PBST, and mounted with ProLong Gold Antifade Reagent (Invitrogen). The following primary antibodies were used: mouse monoclonal anti-otoferlin (HCS-1; Developmental Studies Hybridoma Bank, Iowa City, IA) (1:750); mouse monoclonal anti-Ribeye b (Katie Kindt, National Institutes of Health, Bethesda, MD) (1:10,000); rabbit anti-Vglut3 and LAMP1 (cat #ab23977, ab62562; Abcam, Cambridge, MA) (1:1000).

Staining with mCLING-ATTO 488

Vital dye mCLING-ATTO 488 (cat #710 006AT3; Synaptic Systems, Germany) was used to observe endocytosis in hair cells of WT and mutant zebrafish larvae. Larvae were incubated with 1.7 µM mCLING diluted in embryo media for 6 min at RT and then washed with PBS for 1 min. The duration of the exposure was based on previous studies (Manchanda *et al.*, 2019). Both WT and mutant larvae were exposed to identical conditions with the dye. Samples were fixed for 1.5 h with 4% paraformaldehyde, 0.2% glutaraldehyde on ice, and subsequently for an additional 1.5 h at RT on a shaker as described previously (Revelo *et al.*, 2014). Following a 2 min PBS wash, samples were incubated with a "quenching solution" (100 mM NH_4Cl + 100 mM glycine in PBS) to reduce autofluorescence from unbound/excess aldehydes for 30 min at RT. Samples were washed with PBST for 3 × 5 min and then permeabilized using the immunofluorescence protocol (see above) followed by 3 × 5 min washes with PBST. Finally, samples were incubated with 1:1500 rhodamine-conjugated phalloidin (cat #R415; Thermo Fisher Scientific) in PBS for 1 h at RT and then again washed with PBST 3 × 5 min before mounting with ProLong Gold Antifade Reagent (cat #P36930; Invitrogen) for confocal imaging. Phalloidin was added to stain the apical stereocilia and the actin-rich cuticular plate.

Confocal image acquisition and analysis

Immunofluorescence was performed using a Zeiss LSM 780 NLO confocal laser-scanning microscope fitted with a 63× oil-immersion objective and appropriate filters.

For all imaging experiments, a minimum of $N = 4$ larvae were imaged per genotype, and for each larvae, z-stacks of 4–10 distinct neuromasts were created, beginning at the most apical portion of the neuromast and ending just beyond the basal end of the hair cells. Within each study, all neuromasts were imaged using identical parameters, based on a representative WT neuromast, and with the image having only one neuromast in the viewing area. For HCS-1, Vglut3, and mCLING analysis, maximum intensity projections were created for each z- stack, and the corrected total image fluorescence (CTIF) was calculated using FIJI (an ImageJ-based software): CTIF = IntDen – (Area * Mean of background) (McCloy *et al.*, 2014; Manchanda *et al.*, 2019). The integrated intensity (IntDen) is the product of the mean gray value within the entirety of the image area, and the mean background was measured from a small region of the darkest area of the image.

Ribeye image analysis was conducted by first subtracting the background and subsequently applying the ImageJ Analyse Particle

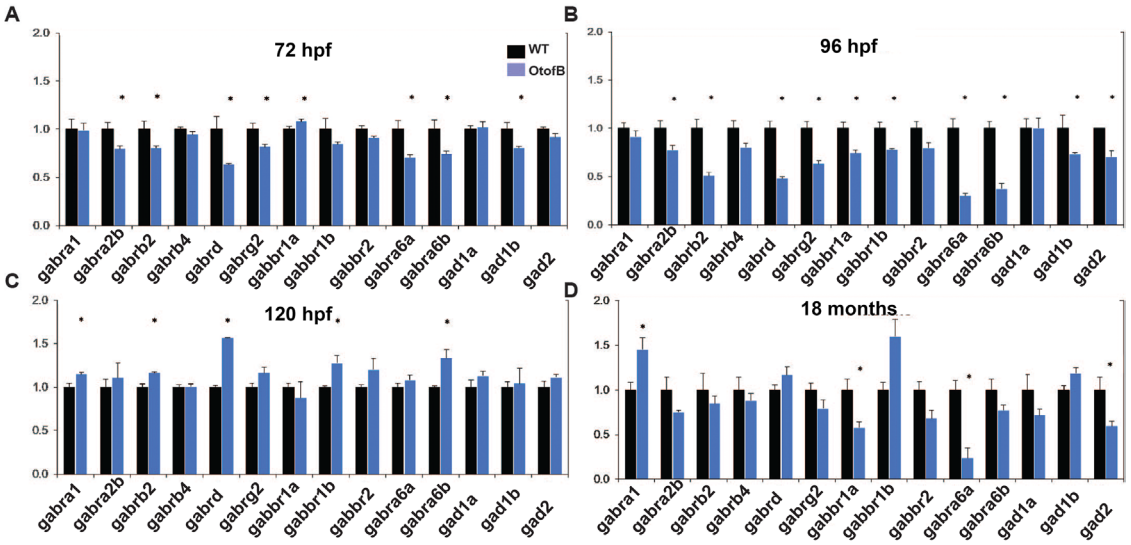

FIGURE 8: The otofB mutation results in abnormal glutamate decarboxylase and GABA receptor subunit transcripts levels. (A–C) Quantification of mRNA by qRT-PCR for GABA receptor subunits and GAD transcripts in wild-type and otofB larvae at 72, 96, and 120 hpf. $N = 4$ for both WT and mutant, with each N as a composite of 20–30 larvae. (D) Quantification of mRNA by qRT-PCR for GABA receptor subunit and GAD transcripts in wild-type and otofB adult zebrafish brain (t test, $p < 0.001$). $N = 4$ for both WT and mutant, with each N as a composite of 20–30 larvae. The data presented are representative of three experimental replicates for each time point. Error bars are SEM.

option, where a relative quantification of size value based on binary black or white pixels in the image under a specified region of interest was calculated. Imaging parameters were maintained the same for each image used as described previously (Manchanda *et al.*, 2019). For the mCLING analysis, the z-stack slices stained with phalloidin were removed from the maximum intensity projections in order to reduce the signal from mCLING associated with the apical kinocilia and stereocilia. Colocalization of proteins was analyzed using ImageJ software and the Pearson's correlation coefficient to quantify the degree of linear dependence of the otoferlin and LAMP1 signals. The value for the correlation ranges from –1 to 1, with a value of 1 corresponding to perfect colocalization. Dual-color images used for the analysis were taken from z-stacks for anti-otoferlin and anti-LAMP1.

Larval zebrafish behavioral analysis

Larval zebrafish behavior was evaluated using two locomotor activity–based assays as previously described: the LPR and the LCR assays (Bugel *et al.*, 2016; Bugel and Tanguay, 2018). For these studies, the ViewPoint Zebrabox system with ZebraLab video tracking software was used (ViewPoint Life Sciences, Lyon, France). WT and otofB mutant zebrafish embryos were reared in 96-well plates until 4 d postfertilization and then evaluated using either the LPR or the LCR assay. The larval zebrafish used in these assays were phenotypically normal.

For the LPR assay, larval zebrafish ($N = 48$ animals per genotype) were subjected to alternating trials of light:dark to evaluate the locomotor response to a photoperiod transition stimulus. The LPR assay consisted of five repeated trials of a 3 min light resting period followed by a 3 min dark stimulation. Statistical differences in locomotor activity between genotypes were evaluated using two approaches: 1) by using the mean activity within each genotype for each minute of the assay, and 2) by using the average activity of each genotype within each photoperiod (3 min average activity).

For the LCR assay, larval zebrafish ($N = 48$ animals per genotype) locomotor activity was evaluated in response to 100 µM PTX (CAS #124-87-8; 98%; Sigma Aldrich, St. Louis, MO). PTX is a model $GABA_A$ receptor antagonist that elicits rapid and robust hyperactive locomotor responses. At 96 hpf, 2 × PTX was prepared in embryo medium and added to achieve a final concentration of 100 µM PTX in 0.1% dimethyl sulfoxide (DMSO) in all treatment and genotype groups. Following the addition of treatment, plates were placed on an illuminated ViewPoint Zebrabox system and locomotor activity was recorded continuously for 3 h. All studies were performed using full illumination to maintain the larvae preference for low levels of locomotor activity observed in normal control animals. Locomotor activity was measured for each minute, providing a time-course response, and activity data weres then binned into 10 min periods. Statistical differences in locomotor responses to PTX between genotypes were evaluated using average activity within each 10 min bin.

Statistics

All data were analyzed with StatPlus v7, except for zebrafish behavior data, which were analyzed using SigmaStat v11. For all imaging studies, a Shapiro–Wilk test for normality and Levene's test for equal variance followed by one-way analysis of variance (ANOVA) were used to assess differences within a given genotype, while a t test was used to assess differences between the genotypes. For qRT-PCR and cell imaging data, t tests were used to compare WT and mutants within a single developmental time period. A Fisher's exact test was used to determine whether the number of inflated swim bladders was different between WT and mutant. For locomotor behavior activity, a Box-Cox power transformation function (MASS R-package) was used to optimally transform activity data for normality before statistical analysis. Two-way repeated measures ANOVA (Tukey's post-hoc) was used to determine significant differences in locomotor activity between treatments (control vs. PTX) and genotypes (WT vs. otofB). A p-value ≤ 0.05 was universally regarded as significantly different for all studies.

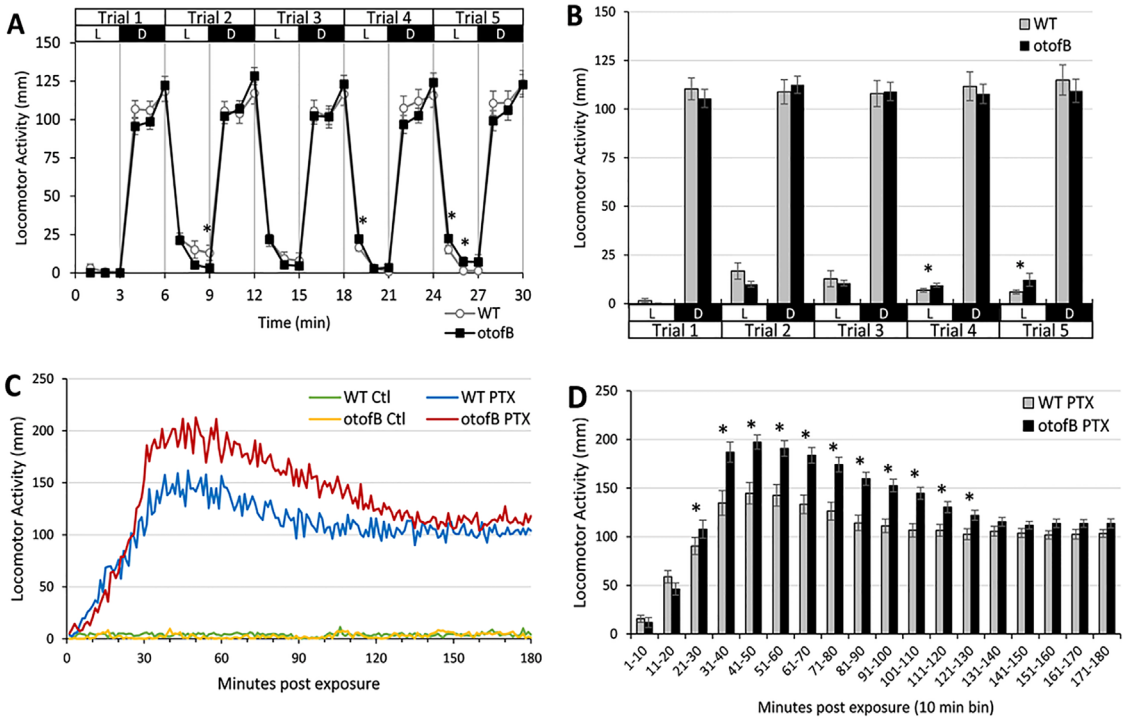

FIGURE 9: Larval zebrafish behavioral assays for wild-type (WT) and otofB mutants at 4 d postefertilization suggest altered behavior and $GABA_A$ receptor function in otofB mutants. (A, B) The larval photomotor response (LPR) assay evaluated locomotor activity in response to repeated photoperiod transitions from light (L) to dark (D), which typically elicits hyperactive responses in the dark phase. Five trials were conducted with 3 min per photoperiod. For the LPR assay, data are shown and statistically analyzed using a time-course plot of average locomotor for (A) each minute, as well as average activity within (B) each 3 min photoperiod. (C, D) The larval chemomotor response (LCR) assay evaluated locomotor activity in response to 100 µM picrotoxin (PTX), a known $GABA_A$ receptor antagonist that elicits a robust hyperactive locomotor response in larval zebrafish. Locomotor activity was measured for 3 h immediately following the application of PTX, relative to control (0.1% DMSO). For the LCR assay, average locomotor activity for each minute is plotted across the 3 h timecourse (C), and data were statistically analyzed using average activity within 10 min time bins (D). All data are reported as mean ± SEM. Significance was determined using two-way repeated measures ANOVA with Tukey's post-hoc, $p \leq 0.05$, $N = 48$ animals per group (4 d postfertilization larval zebrafish).

Cell culture and maintenance

HEK293T cells were cultured in DMEM with 10% fetal bovine serum (Thermo Fisher Scientific) on glass-coated, poly-L-lysine–treated coverslips (for immunofluorescence) and on cell culture dishes (for protein extraction). Media was changed on alternate days, and cells were grown until they were 70–80% confluent, at which point they were transfected using Lipofectamine 3000 (cat L3000001; Thermo Fisher Scientific) according to the manufacturer's protocol. Twenty-four hours after transfection, cells were checked under a fluorescence microscope (Keyence) for the expression of fluorescent proteins.

Cloning of mammalian constructs

For otoferlin-GFP and Oto ΔTMD GFP constructs, cDNA encoding mouse otoferlin, which was a gift from Christine Petit (Institut Pasteur, Paris, France), amplified and ligated to a pcDNA3 GFP LIC cloning vector (6D) which was a gift from Scott Gradia (Addgene) (Addgene plasmid #30127; http://n2t.net/addgene:30127; RRID:Addgene_30127). For otoferlin-GFP, 1–5979 base pairs of the gene was amplified, and for the Oto ΔTMD GFP construct, 1–5655 base pairs of otoferlin was amplified for cloning into the GFP vector. For C2F-TMD-GFP and C2F-GFP constructs, cDNA was amplified from 96 hpf larvae according to the above RNA isolation method. For a N-terminal GFP vector cloning, pcDNA3 LIC cloning vector (6A), which was a gift from Scott Gradia (Addgene plasmid #30124; http://n2t.net/addgene:30124; RRID:Addgene_30124) was used, and GFP was cloned at the N-terminus. This vector was then used to ligate amplicons for cloning.

Immunofluoroscence analysis

HEK293T cells transfected with GFP and CFP-tagged constructs were grown on coverslips. Twenty-four hours later, the coverslips were fixed in 4% Paraformaldehyde in PBS for 10 min and then washed in PBS. For membrane and nuclei staining, the Image-IT LIVE Intracellular Membrane and Nuclear Labeling Kit (Thermo Fisher Scientific) was used. Briefly, to the cells a sufficient amount of labelling solution (wheat germ agglutinin, Alexa Fluor 594 conjugate, and Hoechst 33342 dye) to cover cells adhering to coverslip(s) was added. The cells were then incubated for 10 min at RT. After labeling was complete, the labeling solution was removed and cells were washed twice in Hanks' Balanced Salt solution. After washing, coverslips were mounted in ProLong Gold Antifade Mountant (Thermo Fisher Scientific) for imaging. Images were collected on a Zeiss LSM 780 NLO confocal microscope. Post-imaging processing was performed using Zen black.

Cell fractionation

HEK293T cells transfected with GFP-otoferlin constructs were grown for 24 h. Cells were washed with PBS thrice for 5 min. Cells were then detached using a cell scraper and added to microcentrifuge

tubes kept on ice. These tubes were then centrifuged at 300 rpm for 15 min at 4°C to pellet cells. Cytosolic and membrane fractions were isolated from these cell pellets using the Mem-PER Plus Membrane Protein Extraction Kit (Thermo Fisher Scientific) following the manufacturer's instructions. Isolated protein fractions were snap-frozen at –80°C and later used for Western blot analysis.

Western blot analysis

Cell lysate (50 µg) was loaded to each lane of a 4–20% Mini-PROTEAN TGX Stain-Free Precast Gel (Biorad, USA) for SDS–PAGE and run at constant voltage until the dye front ran out. Then, samples were blotted onto nitrocellulose membranes and blocked with 2% milk in *tris*-buffered saline with Tween (TBST). Proteins were incubated overnight with primary antibodies anti-GFP (Proteintech) and anti-actin (Sigma) at 1:2000. Blots were then washed six times with TBST and incubated with either horseradish peroxidase– or rhodamine-conjugated secondary antibodies at 1:2000. After washing, blots were developed on an Azure c600 Imaging System.

Expression and purification of recombinant otoferlin

pMCSG9 vector containing either mouse otoferlin C2F (1688-1927) or otoferlin C2F-TMD (1711-1992) was transformed into BL21 *Escherichia coli* competent cells. The bacterial cells were grown until OD_{600} and thereafter induced with 0.5 mM Isopropyl β-D-1-thiogalactopyranoside for 16–18 h at 18°C. The cells were lysed in a 20 mM HEPES, 100 mM NaCl buffer with 0.5 mM phenylmethylsulfonyl fluoride, 1–2 µg/ml aprotinin, leupeptin, and pepstatin A, and soluble fraction was incubated with HisPur Ni-NTA Resin (Thermo Fisher Scientific, USA). After binding and washing steps (wash buffer Tris-HCl, 150 mM NaCl, and 20 mM imidazole), the his-tagged protein was eluted with a HEPES buffer containing 200 mM imidazole. The protein concentrations were determined by UV absorbance using extinction coefficients of each protein based on their amino acid sequence. The pMCSG9 vector encodes a cleavage site allowing for the purification tag to be cleaved through treatment with TEV protease.

Recombinant C2F-TMD membrane reconstitution

For membrane reconstitution of the C2F-TMD, 2 mg of recombinant otoferlin was resuspended in a 1% saponin (20 mM Tris, 100 mM NaCl, pH 7.5) solution and added to a 3 mM stock lipid consisting of 25% POPS, 10% POPE, and 65% POPC by mol fraction. The lipid–protein mixture was placed in a 37°C water bath for 30 min, and subsequently a 20 mM Tris, 100 mM NaCl reconstitution buffer was added to the lipid–protein solution to dilute the saponin below the CMC value. The proteoliposome sample was then dialyzed overnight (20 mM Tris, 100 mM NaCl, pH 7.5) to remove saponin. The proteoliposome sample was then centrifuged in an accudenz gradient as described previously (Tucker *et al.*, 2004). The proteoliposomes were collected from the top fraction of the accudenz gradient and analyzed by SDS–PAGE to confirm and quantitate the otoferlin in the proteoliposomes. Assuming no significant loss of lipids in the process, we calculate that the ratio of C2F-TMD:lipid is 1:100. All lipids were from Avanti Lipids (Alabaster, AL).

Protein fluorescence measurements

Steady-state fluorescence measurements were conducted using a QM-40instrument with Glan Thompson polarizers (Photon Technology International, Birmingham, NJ) at 37°C. All fluorescence measurements were conducted in samples containing 20 mM Tris-HCl or HEPES buffer (pH 7.5) with 150 mM NaCl. Reported values represent the mean ± the error for three samples. Each sample was measured multiple times to ensure that it was not changing over time.

Sedimentation assay

For the liposome sedimentation assay, a 1 mM liposome stock containing 25% POPS, 5% PI(4,5)P2, 5% biotin-PE, 5% rhodamine-PE, and 60% POPC was mixed with streptavidin beads and allowed to conjugate for 1 h at RT. The sample was then washed with one volume of 20 mM Tris (pH 7.5) and 100 mM NaCl buffer to remove unbound liposomes. For measurements with the membrane-tethered C2F, the liposome beads were mixed with proteoliposomes with a lipid composition of 25% POPS, 10% POPE, 5% NBD-PE, and 60% POPC and allowed to equilibrate for 1 h at RT with either 100 µM calcium or 1 mM EDTA. For measurements with the soluble C2F, the beads were exposed to 30 µM C2F and liposomes with a lipid composition of 25% POPS, 10% POPE, 5% NBD-PE, and 60% POPC and allowed to equilibrate for 1 h at RT with either calcium or EDTA. The beads were then pelleted and the NBD fluorescence intensity for soluble and insoluble fractions was measured using a QM-40instrument. The ratio of the intensities was then plotted for each sample. The intensity of the rhodamine fluorescence was also measured and compared to ensure that there were no variations in the amount of biotinylated liposomes in the bead samples. SDS–PAGE was run to confirm the presence of protein in the supernatant and pellet fractions. All lipids were from Avanti Lipids (Alabaster, AL).

ACKNOWLEDGMENTS

We thank Rebecca France for help creating otoferlin expression constructs. This work was supported by National Institute of Deafness and Other Communication Disorders Grant 1R01DC014588.

REFERENCES

Abdullah N, Padmanarayana M, Marty NJ, Johnson CP (2014). Quantitation of the calcium and membrane binding properties of the C2 domains of dysferlin. Biophys J 106, 382–389.

Akil O, Dyka F, Calvet C, Emptoz A, Lahlou G, Nouaille S, Boutet de Monvel J, Hardelin JP, Hauswirth W, Avan P, *et al.* (2019). Dual AAV-mediated gene therapy restores hearing in a DFNB9 mouse model. Proc Natl Acad Sci USA 116, 4496–4501.

Bonventre JA, Holman C, Manchanda A, Codding SJ, Chau T, Huegel J, Barton C, Tanguay R, Johnson CP (2019). Fer1l6 is essential for the development of vertebrate muscle tissue in zebrafish. Mol Biol Cell 30, 293–301.

Bugel SM, Bonventre JA, Tanguay RL (2016). Comparative developmental toxicity of flavonoids using an integrative zebrafish system. Toxicol Sci 154, 55–68.

Bugel SM, Tanguay RL (2018). Multidimensional chemobehavior analysis of flavonoids and neuroactive compounds in zebrafish. Toxicol Appl Pharmacol 344, 23–34.

Cepeda AP, Jung SY, Moser T, Reisinger E, Al-Moyed H, Kügler S (2018). A dual-AAV approach restores fast exocytosis and partially rescues auditory function in deaf otoferlin knock-out mice. EMBO Mol Med 11, e9396.

Chatterjee P, Padmanarayana M, Abdullah N, Holman CL, LaDu J, Tanguay RL, Johnson CP (2015). Otoferlin deficiency in zebrafish results in defects in balance and hearing: rescue of the balance and hearing phenotype with full-length and truncated forms of mouse otoferlin. Mol Cell Biol 35, 1043–1054.

Chen Y, Wang YH, Zheng Y, Li M, Wang B, Wang QW, Fu CL, Liu YN, Li X, Yao J (2021). Synaptotagmin-1 interacts with PI(4,5)P2 to initiate synaptic vesicle docking in hippocampal neurons. Cell Rep 34, 108842.

Cocco A, Carolina Rönnberg AM, Jin Z, André GI, Vossen LE, Bhandage AK, Thörnqvist PO, Birnir B, Winberg S (2017). Characterization of the γ-aminobutyric acid signaling system in the zebrafish (Danio Rerio Hamilton) central nervous system by reverse transcription-quantitative polymerase chain reaction. Neuroscience 343, 300–321.

Duncker SV, Franz C, Kuhn S, Schulte U, Campanelli D, Brandt N, Hirt B, Fakler B, Blin N, Ruth P, *et al*. (2013). Otoferlin couples to clathrin-mediated endocytosis in mature cochlear inner hair cells. J Neurosc 33, 9508–9519.
Fettiplace R (2017). Hair cell transduction, tuning, and synaptic transmission in the mammalian cochlea. Compr Physiol 7, 1197–1227.
Hams N, Padmanarayana M, Qiu W, Johnson CP (2017). Otoferlin Is a Multivalent Calcium-Sensitive Scaffold Linking SNAREs and Calcium Channels. Proc Natl Acad Sci USA 4, 8023–8028.
Heidrych P, Zimmermann U, Kuhn S, Franz C, Engel J, Duncker SV, Hirt B, Pusch C, Ruth P, Pfister M, *et al*. (2009). Otoferlin interacts with myosin VI: implications for maintenance of the basolateral synaptic structure of the inner hair cell. Hum Mol Genet 18, 2779–2790.
Johnson CP, Chapman ER (2010). Otoferlin is a calcium sensor that directly regulates SNARE-mediated membrane fusion. J Cell Biol 191, 187–197.
Jung SY, Maritzen T, Wichmann C, Jing Z, Neef A, Revelo NH, Al-Moyed H, Meese S, Wojcik S, Panou I, *et al*. (2015). Disruption of adaptor protein 2μ (AP-2μ) in cochlear hair cells impairs vesicle reloading of synaptic release sites and hearing. EMBO J 34, 2686–2702.
Kindt KS, Sheets L (2018). Transmission disrupted: modeling auditory synaptopathy in zebrafish. Front Cell Dev Biol 6, 114.
Kurowska M, Daszkowska-Golec A, Gruszka D, Marzec M, Szurman M, Szarejko I, Maluszynski M (2011). TILLING—a shortcut in functional genomics. J Appl Genet 52, 371–390.
Lee J, Littleton JT (2015). Transmembrane tethering of synaptotagmin to synaptic vesicles controls multiple modes of neurotransmitter release. Proc Natl Acad Sci USA 112, 3793–3798.
Lek A, Evesson FJ, Lemckert FA, Redpath GMI, Lueders A-K, Turnbull L, Whitchurch CB, North KN, Cooper ST (2013). Calpains, cleaved mini-dysferlinC72, and L-type channels underpin calcium-dependent muscle membrane repair. J Neurosci 33, 5085–5094.
Lek A, Evesson FJ, Sutton RB, North KN, Cooper ST (2012). Ferlins: regulators of vesicle fusion for auditory neurotransmission, receptor trafficking and membrane repair. Traffic.
Manchanda A, Chatterjee P, Bonventre JA, Haggard DE, Kindt KS, Tanguay RL, Johnson CP (2019). Otoferlin depletion results in abnormal synaptic ribbons and altered intracellular calcium levels in zebrafish. Sci Rep 9, 14273.
Marty NJ, Holman CL, Abdullah N, Johnson CP (2013). The C2 domains of otoferlin, dysferlin, and myoferlin alter the packing of lipid bilayers. Biochemistry 52, 5585–5592.
McCloy RA, Rogers S, Elizabeth Caldon C, Lorca T, Castro A, Burgess A (2014). Partial inhibition of Cdk1 in G2 phase overrides the SAC and decouples mitotic events. Cell Cycle 13, 1400–1412.
Michalski N, Goutman JD, Auclair SM, de Monvel JB, Tertrais M, Emptoz A, Parrin A, Nouaille S, Guillon M, Sachse M, *et al*. (2017). Otoferlin acts as a Ca2+sensor for vesicle fusion and vesicle pool replenishment at auditory hair cell ribbon synapses. eLife 6, e31013.
Moser T, Grabner CP, Schmitz F (2020). Sensory processing at ribbon synapses in the retina and the cochlea. Physiol Rev 100, 103–144.
Noh J, Seal RP, Garver JA, Edwards RH, Kandler K (2010). Glutamate co-release at GABA/glycinergic synapses is crucial for the refinement of an inhibitory map. Nat Neurosci 13, 232–238.
Padmanarayana M, Hams N, Speight LC, Petersson EJ, Mehl RA, Johnson CP (2014). Characterization of the lipid binding properties of otoferlin reveals specific interactions between PI(4,5)P2 and the C2C and C2F domains. Biochemistry 53, 5023–5033.
Pangršič T, Lasarow L, Reuter K, Takago H, Schwander M, Riedel D, Frank T, Tarantino L, Bailey J, Strenzke N, *et al*. (2010). Hearing requires otoferlin-dependent efficient replenishment of synaptic vesicles in hair cells. Nat Neurosci 13, 869–876.
Perry J, Welham T, Cheminant S, Parniske M, Wang T (2005). Tilling. In: Lotus Japonicus Handbook, 197–210. doi:10.1007/1-4020-3735-X_20.
Pfaffl MW (2001). A new mathematical model for relative quantification in real-time RT-PCR. Nucleic Acids Res 29, e45.
Ramakrishnan NA, Drescher MJ, Drescher DG (2009). Direct interaction of otoferlin with syntaxin 1A, SNAP-25, and the L-type voltage-gated calcium channel Ca v1.3. J Biol Chem 284, 1364–1372.
Rankovic V, Vogl C, Dörje NM, Bahader I, Duque-Afonso CJ, Thirumalai A, Weber T, Kusch K, Strenzke N, Moser T (2021). Overloaded adeno-associated virus as a novel gene therapeutic tool for otoferlin-related deafness. Front Mol Neurosci 13, 600051.
Revelo NH, Kamin D, Truckenbrodt S, Wong AB, Reuter-Jessen K, Reisinger E, Moser T, Rizzoli SO (2014). A new probe for super-resolution imaging of membranes elucidates trafficking pathways. J Cell Biol 205, 591–606.
Roux I, Safieddine S, Nouvian R, Grati M, Simmler MC, Bahloul A, Perfettini I, Le Gall M, Rostaing P, Hamard G, *et al*. (2006). Otoferlin, defective in a human deafness form, is essential for exocytosis at the auditory ribbon synapse. Cell 127, 277–289.
Safieddine S, El-Amraoui A, Petit C (2012). The auditory hair cell ribbon synapse: from assembly to function. Annu Rev Neurosci 35, 509–528.
Sarro EC, Kotak VC, Sanes DH, Aoki C (2008). Hearing loss alters the subcellular distribution of presynaptic GAD and postsynaptic GABAA receptors in the auditory cortex. Cereb Cortex 18, 2855–2867.
Sonnhammer EL, von Heijne G, Krogh A (1998). A hidden Markov model for predicting transmembrane helices in protein sequences. Int Conf Intell Syst Mol Biol 6, 175–182.
Tertrais M, Bouleau Y, Emptoz A, Belleudy S, Sutton RB, Petit C, Safieddine S, Dulon D (2019). Viral transfer of mini-otoferlins partially restores the fast component ofexocytosis and uncovers ultrafast endocytosis in auditory hair cells ofotoferlin knock-out mice. J. Neurosci 39, 3394–3411.
Tucker WC, Weber T, Chapman ER (2004). Reconstitution of Ca2+-regulated membrane fusion by synaptotagmin and SNAREs. Science 304, 435–438.
Vogl C, Cooper BH, Neef J, Wojcik SM, Reim K, Reisinger E, Brose N, Rhee J-S, Moser T, Wichmann C (2015). Unconventional molecular regulation of synaptic vesicle replenishment in cochlear inner hair cells. J Cell Sci 128, 638–644.
Westerfield M (2007). The Zebrafish Book. A Guide for the Laboratory Use of Zebrafish (Danio Rerio), 5th ed., Eugene: University of Oregon Press.
Wienholds E, van Eeden F, Kosters M, Mudde J, Plasterk RHA, Cuppen E (2003). Efficient target-selected mutagenesis in zebrafish. Genome Res 13, 2700–2707.
Wu W, Rahman MN, Guo J, Roy N, Xue L, Cahill CM, Zhang S, Jia Z (2015). Function coupling of otoferlin with GAD65 acts to modulate GABAergic activity. J Mol Cell Biol 7, 168–179.
Yasunaga S, Grati M, Cohen-Salmon M, El-Amraoui A, Mustapha M, Salem N, El-Zir E, Loiselet J, Petit C (1999). A mutation in OTOF, encoding otoferlin, a FER-1-like protein, causes DFNB9, a nonsyndromic form of deafness. Nat Genet 21, 363–369.